
A Systematic Study of Evolved Supernova Remnants in the Large and Small Magellanic Clouds with Suzaku

Yoko TAKEUCHI^{1,2*}, Hiroya YAMAGUCHI^{3,4}, and Toru TAMAGAWA²

¹Department of Physics, Tokyo University of Science, 3-1 Kagurazaka, Shinjuku-ku, Tokyo 162-8601, Japan

²RIKEN Nishina Center, 2-1 Hirosawa, Wako, Saitama, 351-0198, Japan

³NASA Goddard Space Flight Center, Code 662, Greenbelt, MD 20771, USA

⁴Department of Astronomy, University of Maryland, College Park, MD 20742, USA

*E-mail: takeuchi@crab.riken.jp

Received ; Accepted

Abstract

Typing the origin (i.e., Type Ia or core-collapse) of supernova remnants (SNRs) is crucial to determine the rates of supernova (SN) explosions in a galaxy, which is a key to understand its recent chemical evolution. However, evolved SNRs in the so-called Sedov phase are dominated by the swept-up interstellar medium (ISM), making it difficult to determine their ejecta composition and thus SN type. Here we present a systematic X-ray study of nine evolved SNRs in the Magellanic Clouds, DEM L238, DEM L249, 0534–69.9, 0548–70.4, B0532–71.0, B0532–67.5, 0103–72.6, 0049–73.6, and 0104–72.3, using archival data of the Suzaku satellite. Although Suzaku does not spatially resolve the SN ejecta from the swept-up ISM due to the limited angular resolution, its excellent energy resolution has enabled clear separation of emission lines in the soft X-ray band. This leads to the finding that the ‘spatially-integrated’ spectra of the evolved ($\sim 10^4$ yr) SNRs are still significantly contributed by emission from the ejecta at the energies around 1 keV. The Fe/Ne mass ratios, determined mainly from the well-resolved Fe L-shell and Ne K-shell lines, clearly divide the observed SNRs into the Type Ia and core-collapse groups, confirming some previous typing made by Chandra observations that

Table 1. List of the Magellanic SNRs we analyze in this work.

| Name | Suzaku Obs. ID | Exposure (ks) | Date of Observation | Position (J2000) | | Radius (arcsec / pc) | Age (kyr) | Ref.* |
|-------------------------|----------------|------------------|---------------------|---|--|-------------------------|--------------|-------|
| | | | | R.A. | Decl. | | | |
| LMC SNRs: | | | | | | | | |
| DEM L238 [†] | 505063010 | 200 | 2010 Apr 22 | 05 ^h 34 ^m 24 ^s | −70 ^d 33 ^m 12 ^s | 80/ 20 | 13.5 | 1 |
| DEM L249 [†] | 505063010 | 200 | 2010 Apr 22 | 05 ^h 36 ^m 13 ^s | −70 ^d 38 ^m 10 ^s | ~80/ ~20 | 10–15 | 1 |
| 0534–69.9 | 505064010 | 109 | 2010 Mar 31 | 05 ^h 34 ^m 01 ^s | −69 ^d 54 ^m 22 ^s | 57 / 13.7 | 10.1 | 2 |
| 0548–70.4 | 505065010 | 104 | 2010 July 1 | 05 ^h 74 ^m 52 ^s | −70 ^d 25 ^m 01 ^s | 51 / 12.1 | 7.1 | 2 |
| B0532–71.0 | 803038010 | 49 | 2008 Apr 28 | 05 ^h 31 ^m 59 ^s | −71 ^d 00 ^m 03 ^s | 87/ 21 | 23–27 | 3 |
| B0532–67.5 [‡] | 806007010 | 82 | 2011 Nov 6 | 05 ^h 32 ^m 23 ^s | −67 ^d 31 ^m 16 ^s | 48/11.6 | — | — |
| SMC SNRs: | | | | | | | | |
| 0103–72.6 | 501077010 | 49 | 2006 Apr 23 | 01 ^h 05 ^m 07 ^s | −72 ^d 23 ^m 10 ^s | 85 / 24.7 | 18 | 4 |
| 0049–73.6 | 503094010 | 120 | 2008 June 12 | 00 ^h 51 ^m 09 ^s | −73 ^d 21 ^m 54 ^s | 72 / 20.5 | 14 | 5 |
| 0104–72.3 | 803002010 | 107 | 2008 May 15 | 01 ^h 06 ^m 19 ^s | −72 ^d 05 ^m 41 ^s | 55 / 16 | 17.6 | 6 |

* Representative references — (1) Borkowski et al. (2006); (2) Hendrick et al. (2003); (3) Williams et al. (2005); (4) Park et al. (2003a); (5) Hendrick et al. (2005);

(6) Lopez et al. (2014)

[†] These two SNRs were observed in the same FoV.

[‡] The age of B0532–67.5 is previously unreported.

had utilized its extremely high angular resolution. This demonstrates that spatially-integrated X-ray spectra of old SNRs can also be used to discriminate their progenitor type, which would be helpful for future systematic studies of extragalactic SNRs with ASTRO-H and beyond.

Key words: ISM: supernova remnants — ISM: abundances — X-rays: ISM — Magellanic Clouds

1 Introduction

A supernova (SN) explosion provides heavy elements synthesized during the stellar evolution or the explosion itself to the interstellar space efficiently. There are two distinct types of SNe: thermonuclear (Type Ia) explosions of a white dwarf(s) and core-collapse (CC) explosions of a massive star. Since the major nucleosynthesis products of both SN types are largely different from each other, it is crucial to determine their explosion rates in an individual galaxy to reveal its recent chemical enrichment history. X-ray observations of young supernova remnants (SNRs) allow us to distinguish their parent SN types, as their X-ray spectrum is dominated by emission from the ejecta (e.g., Vink 2012). The SN rate in the Large Magellanic Cloud (LMC), the nearest extra-galaxy to us and hence the best object

for a comprehensive study of a galactic chemical evolution, was estimated using ASCA data of young ($t \lesssim 1,500$ yr) LMC SNRs (Hughes et al. 1995).

On the other hand, typing the origin of an evolved ($t \gtrsim 5,000$ yr) SNR is often very challenging, because the X-ray spectrum integrated from the entire SNR is dominated by the swept-up interstellar medium (ISM). In fact, previous ASCA and XMM-Newton observations of Magellanic Sedov-phase SNRs were utilized for studying the ISM abundances (e.g., Hughes et al. 1998; van der Heyden et al. 2004). A breakthrough was achieved by the extremely high angular resolution ($\sim 0''.5$) of the Chandra X-ray Observatory. Allowing us to spatially resolve the ejecta core from the swept-up ISM shell, Chandra has successfully distinguished the progenitor types of a number of evolved SNRs in the Magellanic Clouds (e.g., DEM L71: Hughes et al. 2003; N49B: Park et al. 2003b; N132D: Borkowski et al. 2007).

However, opportunities for the spatially-resolved analysis are limited, since it requires both an expensive telescope with an adequate angular resolution and a target with a reasonable angular size. Although the forthcoming X-ray mission ASTRO-H (Takahashi et al. 2014) will be dramatically changing our view of SNRs with its excellent spectral resolution ($\Delta E \sim 5$ eV at 0.5–10 keV), its half power diameter of $1'.3$ is larger than the typical angular size of evolved SNRs in the Magellanic Clouds ($\sim 1'$). Moreover, SNRs in nearby spiral galaxies (e.g., M31) cannot be resolved into ejecta and ISM components even with the Chandra's angular resolution. It is, therefore, important to identify a simple (but reliable) diagnostic to distinguish SN types from integrated X-ray spectra alone. It would be worth noting that recent Suzaku observations of the middle-aged ($t \sim 5,000$ yr) LMC SNRs DEM L71 and N49B robustly confirmed their abundance enhancement (Fe and Mg, respectively), which was originally revealed by the preceding Chandra observations, even from the spectra of the entire remnants (Uchida et al. 2015). This was enabled due to the high sensitivity (to emission lines) of the X-ray Imaging Spectrometer (XIS: Koyama et al. 2007) on board Suzaku.

In this paper, we focus on even more evolved ($t \gtrsim 10,000$ yr) SNRs in the LMC and the Small Magellanic Clouds (SMC), DEM L238, DEM L249, 0534–69.9, 0548–70.4, B0532–71.0, B0532–67.5, 0103–72.6, 0049–73.6, and 0104–72.3 (table 1), observed by the Suzaku XIS. The progenitor type of most of these objects has been proposed by previous Chandra studies based on their spatially-resolved spectra (see §4.1). The aim of our present work is not to investigate the detailed nature of each individual object nor to understand the detailed evolutionary characteristics of Sedov-phase SNRs, but to demonstrate that spatially-integrated X-ray spectra of the evolved SNRs can still be used to distinguish their progenitor type, based on an independent analysis of the high-quality Suzaku data. This not only strengthens (or competes with) the previous typing made by Chandra but also identifies a key spectral feature that immediately distinguishes an SN type, which should be useful for the future

spectroscopy of extra galaxies. To achieve this goal, we systematically analyze the nine evolved SNRs with uniform data reduction and spectral models. Such an approach (i.e., uniform analysis) is known to be a reliable way for the progenitor type discrimination (e.g., Lopez et al. 2011; Yamaguchi et al. 2014).

In §2, we describe the observations and data reduction. The results of the spectral analysis are presented in §3, and discussed in §4. Finally, we conclude this work in §5. We assume 50 kpc and 60 kpc for the distances to the LMC and SMC, respectively (Westerlund 1990).

2 Observations and Data Reduction

We analyzed archival data of the nine SNRs taken by the Suzaku/XIS, of which observation details are summarized in table 1. The XIS consists of four X-ray charge-coupled devices (CCDs). Three of them (XIS0, XIS2, and XIS3) are front-illuminated (FI) and the other (XIS1) is back-illuminated (BI). The former has a better energy response and a lower background level, while the latter has superior sensitivity in the soft X-ray band. Combined with X-Ray Telescopes (XRTs; Serlemitsos et al. 2007), the field of view (FoV) of the XISs, which are identical among the four chips, covers an $\sim 18' \times 18'$ region with a half-power diameter (HPD) of $\sim 2'$. We used all the CCD data for the analysis, but the XIS2 was out of operation during the observations of other than 0103–72.6, possibly caused by the impact of a micrometeorite.

For data reduction, we used the HEASoft version 16.6 software package. We reprocessed the data using the `aepipeline` task with the latest calibration data released in May 2015. The good time interval screening was performed in accordance with the standard criteria, obtaining the effective exposures given in table 1.

For each SNR, we extracted XIS spectra from a circular region centered at the source with a diameter of $\sim 4'$. A background spectrum was extracted from an annular region surrounding the source with inner and outer diameters of $12'$ and $16'$, respectively. We attempted several different background regions, and confirmed no significant change in the measured spectral parameters. We created XIS redistribution matrix files (RMFs) and ancillary response files (ARFs) using the `xisrmfgen` and `xissimarfgen` tasks. The following spectral analysis was performed with the XSPEC software version 12.8.2 (Arnaud 1996).

3 Analysis and Results

Figure 1 shows the XIS spectra of all the SNRs. The K-shell emission of O, Ne, Mg, and Si, and/or the Fe L-shell emission are clearly separated in most spectra. Since none of the SNRs shows a significant

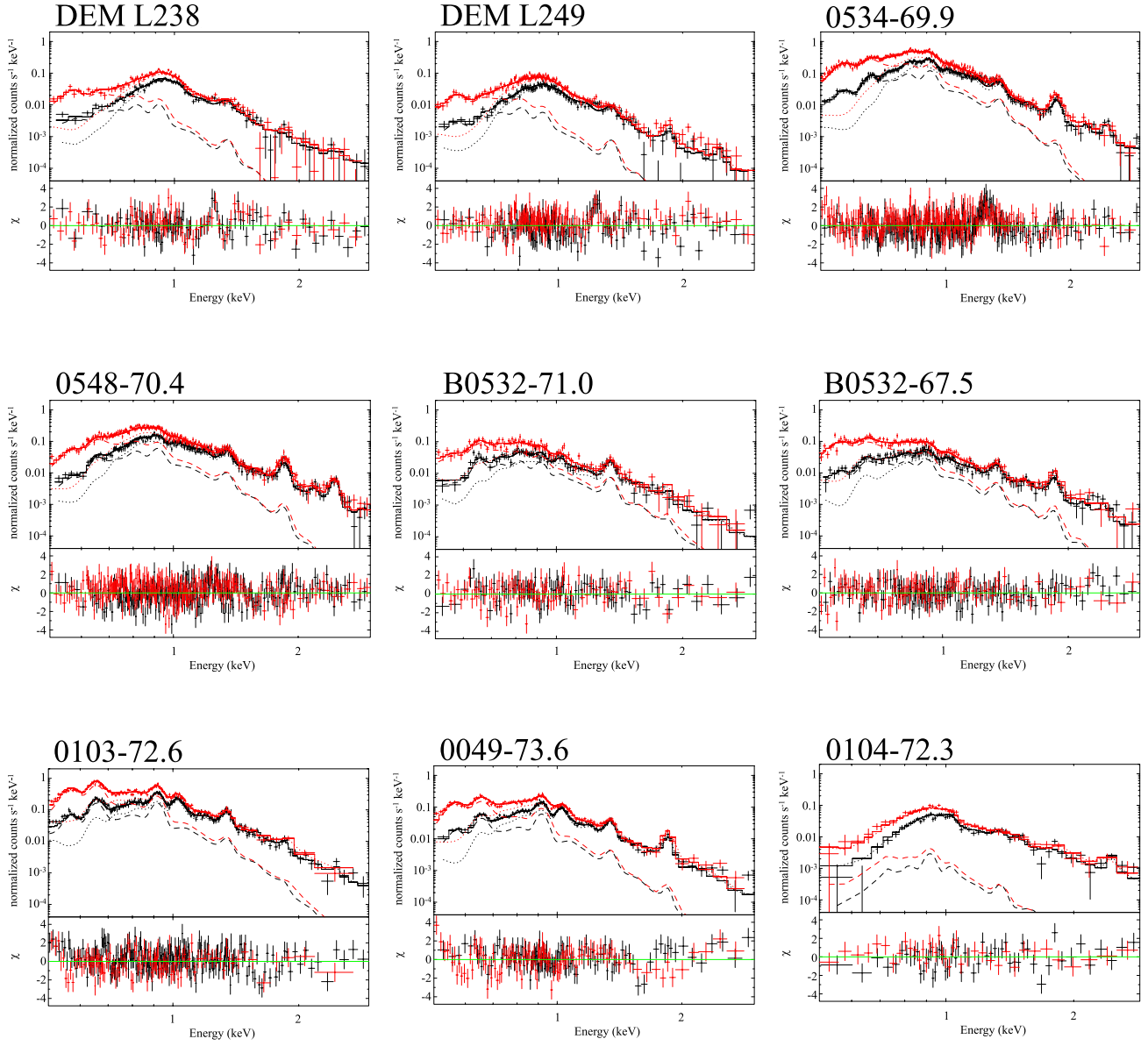


Fig. 1. Suzaku XIS spectra of the Magellanic SNRs fitted with the best-fit models given in table 2. The black and red data points represent the XIS F1 and BI CCDs, respectively. The best-fit models are indicated by the dashed and dotted lines.

signal above ~ 3 keV, we focus on the 0.5–3.0 keV data for the following spectral analysis. Here we perform an unbiased spectral modeling although the previous Chandra observations had revealed a degree of chemical inhomogeneity in some SNRs. We first fit the spectra with a single-component variable-abundance non-equilibrium ionization (VNEI) plasma model based on the *AtomDB*¹ version 3.0.2. The free parameters were the electron temperature (kT_e), ionization parameter ($n_e t$, where n_e

¹ <http://www.atomdb.org/index.php>

and t are the electron density and elapsed time since the gas was shock heated), emission measure (EM), and the abundances of O, Ne, Mg, Si, S, and Fe. For several SNRs, however, we fixed the O, Si, and/or S abundances to the mean LMC/SMC ISM values of Russell & Dopita (1992) or Lewis et al. (2003), because otherwise the fit did not converge. The abundances of the other elements were also fixed to the mean ISM values, but the Ni was tied to Fe. The interstellar extinction in the Galaxy and Magellanic Clouds was separately considered. The Galactic absorption column density with the solar abundances was fixed at $N_{\text{H}}^{\text{Gal}} = 6 \times 10^{20} \text{ cm}^{-2}$, based on the Galactic HI observations of Dickey & Lockman (1990). The other component (N_{H}^{MC}) was a free parameter, with the assumption of the LMC/SMC metal abundances (using the *phabs* model in XSPEC).

This model and assumptions yielded reasonable fits with $\chi_{\nu}^2 \sim 1.2\text{--}2.0$, but introducing a two-temperature NEI model resulted in a significantly better fits for all the SNRs other than 0104–72.3. We allowed kT_e and $n_e t$ of the two components to vary independently, but the elemental abundances were linked between them. Typical electron temperatures of the high- kT_e and low- kT_e components were 0.5–1.0 keV and 0.2–0.3 keV, respectively. The ionization parameter of the low- kT_e component was derived to be very high ($\gtrsim 10^{12} \text{ cm}^{-3} \text{ s}$) in most SNRs, suggesting that this component is almost in the collisional ionization equilibrium (CIE). In this case, we fixed $n_e t$ to $1 \times 10^{13} \text{ cm}^{-3} \text{ s}$, where the plasma is considered to be in the full CIE state. The best-fit parameters we obtained are given in table 2. Only in 0104–72.3, the second component with a free electron temperature did not improve the fit at all. Nevertheless, we attempted modeling with the two components by fixing the low- kT_e value to 0.3 keV, to determine the upper limit of the low- kT_e emission measure. We give in table 2 the results from both 1- kT_e and 2- kT_e modelings, showing no difference in the derived elemental abundances. Similarly, we confirmed that the 1-component fit did not alter the abundance pattern for the other SNRs when this model gave reasonable results with $\chi_{\nu}^2 \lesssim 1.5$. We also fit the data of all the SNRs assuming the LMC/SMC abundances for the low- kT_e component, but the abundances of the other component did not change significantly from the values listed in table 2.

The best-fit models and residuals are shown in figure 1. In the first four spectra (DEML238, DEML249, 0534–69.9, and 0548–70.4), apparent disagreement between the data and model is seen at the energies around 1.2 keV. Given that the large residuals are found only in the Fe-rich remnants (see table 2), this feature is likely to be associated with Fe L-shell emission. In fact, similar residuals were reported in a number of previous works (e.g., Brickhouse et al. 2000; Uchida et al. 2015), and interpreted as Fe L-shell transitions from high quantum numbers ($n > 5$) which are missing from the present plasma code. If we add a Gaussian to compensate these missing lines, the χ_{ν}^2 values are significantly reduced, but no change is confirmed in the other best-fit parameters.

Table 2. The best-fit spectral parameters

| Parameters | DEM L238 | DEM L249 | 0534-69.9 | 0548-70.4 | B0532-71.0 | B0532-67.5 | 0103-72.6 | 0049-73.6 | 0104-72.3 (1- kT_e) | 0104-72.3 (2- kT_e) |
|---------------------------------|------------------|------------------|------------------|------------------|------------------|------------------|------------------|------------------|------------------------|------------------------|
| N^{MC}_H * | $0.0^{+6.3}$ | $4.3^{+13.8}$ | $34.2^{+11.8}$ | 49^{+12} | $0.16^{+9.07}$ | $8.2^{+22.5}$ | $0.0^{+1.2}$ | $0.0^{+1.3}$ | 0^{+13} | $0.45^{+12.83}$ |
| H | -0.0 | -4.3 | -3.6 | -11 | -0.16 | -8.2 | -0.0 | -0.0 | -0 | -0.45 |
| (High temperature component) | | | | | | | | | | |
| kT_e | $1.05^{+0.10}$ | $0.86^{+0.14}$ | $0.68^{+0.03}$ | $0.68^{+0.04}$ | $0.63^{+0.15}$ | $0.73^{+0.25}$ | $0.52^{+0.04}$ | $0.63^{+0.03}$ | $0.87^{+0.02}$ | $0.88^{+0.05}$ |
| $n_e t^\dagger$ | $1.16^{+0.72}$ | $2.06^{+1.58}$ | $1.47^{+0.48}$ | $1.53^{+0.99}$ | $2.44^{+9.21}$ | $1.09^{+3.37}$ | $3.34^{+4.84}$ | $1.81^{+0.51}$ | 100 (fixed) | 100 (fixed) |
| EM ‡ | $2.77^{+1.14}$ | $2.35^{+0.99}$ | $20.4^{+3.9}$ | $26.0^{+5.0}$ | $13.4^{+10.2}$ | $10.2^{+7.2}$ | 54^{+35} | $11.3^{+2.6}$ | $9.4^{+2.1}$ | $9.2^{+2.2}$ |
| | -0.90 | -0.90 | -2.9 | -3.7 | -4.6 | -3.9 | -11 | -2.3 | -2.2 | -2.1 |
| (Low temperature component) | | | | | | | | | | |
| kT_e | $0.172^{+0.005}$ | $0.173^{+0.018}$ | $0.169^{+0.003}$ | $0.181^{+0.007}$ | $0.259^{+0.035}$ | $0.277^{+0.153}$ | $0.202^{+0.011}$ | $0.186^{+0.007}$ | — | 0.3 (fixed) |
| | -0.005 | -0.012 | -0.008 | -0.006 | -0.034 | -0.089 | -0.009 | -0.004 | — | — |
| $n_e t^\dagger$ | 100 (fixed) | $10.24^{+9.3}$ | 100 (fixed) | 100 (fixed) | 100 (fixed) | $0.89^{+3.3}$ | 100 (fixed) | 100 (fixed) | — | 100 (fixed) |
| | | | | | | -0.84 | | | | |
| EM ‡ | 31^{+27} | 26^{+48} | 670^{+590} | 310^{+200} | 41^{+21} | 33^{+157} | 153^{+30} | 52^{+14} | — | $0.66^{+3.94}$ |
| | -16 | -15 | -250 | -130 | -15 | -29 | -23 | -11 | | -0.66 |
| (Abundances) | | | | | | | | | | |
| O | $0.22^{+0.24}$ | $0.25^{+0.38}$ | $0.29^{+0.06}$ | $0.31^{+0.13}$ | 0.263 (fixed) | 0.263 (fixed) | $0.36^{+0.07}$ | $0.51^{+0.15}$ | 0.126 (fixed) | 0.126 (fixed) |
| | -0.12 | -0.13 | -0.08 | -0.04 | | | -0.06 | -0.11 | | |
| Ne | $0.57^{+0.38}$ | $0.47^{+0.41}$ | $0.41^{+0.11}$ | $0.38^{+0.1}$ | $0.25^{+0.12}$ | $0.27^{+0.09}$ | $0.62^{+0.13}$ | $1.09^{+0.27}$ | $1.5^{+0.81}$ | $1.47^{+0.84}$ |
| | -0.32 | -0.36 | -0.09 | -0.07 | -0.06 | -0.04 | -0.06 | -0.19 | -0.59 | -0.77 |
| Mg | $0.60^{+0.50}$ | $0.96^{+0.99}$ | $0.52^{+0.13}$ | $0.45^{+0.14}$ | $0.61^{+0.12}$ | $0.27^{+0.08}$ | $0.37^{+0.09}$ | $0.71^{+0.18}$ | $0.57^{+0.39}$ | $0.57^{+0.4}$ |
| | -0.26 | -0.45 | -0.09 | -0.08 | -0.15 | -0.07 | -0.06 | -0.14 | -0.26 | -0.27 |
| Si | $0.18^{+0.3}$ | $0.74^{+0.81}$ | $0.76^{+0.19}$ | $0.97^{+0.25}$ | 0.309 (fixed) | $0.66^{+0.25}$ | $0.21^{+0.06}$ | $1.25^{+0.3}$ | $0.26^{+0.23}$ | $0.26^{+0.23}$ |
| | -0.18 | -0.25 | -0.15 | -0.15 | | -0.16 | -0.07 | -0.24 | -0.17 | -0.18 |
| S | 0.309 (fixed) | $1.12^{+0.94}$ | $0.70^{+0.33}$ | $1.75^{+0.49}$ | 0.309 (fixed) | $0.59^{+0.72}$ | $0.24^{+0.72}$ | 0.24 (fixed) | $1.24^{+0.72}$ | $1.24^{+0.72}$ |
| | | -0.91 | -0.31 | -0.34 | | -0.45 | -0.45 | | -0.53 | -0.53 |
| Fe | $1.62^{+0.81}$ | $1.96^{+1.13}$ | $1.12^{+0.23}$ | $0.60^{+0.17}$ | $0.17^{+0.06}$ | $0.16^{+0.05}$ | $0.10^{+0.01}$ | $0.32^{+0.09}$ | $0.36^{+0.12}$ | $0.36^{+0.13}$ |
| | -0.48 | -0.65 | -0.18 | -0.11 | -0.05 | -0.04 | -0.04 | -0.07 | -0.07 | -0.08 |
| Flux § | 5.56 | 5.00 | 27.5 | 14.5 | 8.75 | 7.73 | 27.6 | 12.9 | 3.51 | 3.53 |
| $L_{0.5-3\text{keV}}^\parallel$ | 1.66 | 1.50 | 8.23 | 4.34 | 2.62 | 2.31 | 11.9 | 5.56 | 1.51 | 1.52 |
| $\chi^2_\nu(d.o.f)$ | 1.41 (168) | 1.25 (261) | 1.26 (478) | 1.22 (465) | 1.16 (170) | 1.00 (240) | 1.31 (323) | 1.30 (208) | 1.19(88) | 1.20 (87) |

The uncertainties are in the 90% confidence range.

* The unit is 10^{20} cm^{-2} .

† The unit is $10^{11} \text{ cm}^{-3} \text{ s}$.

‡ The unit is 10^{57} cm^{-3} .

§ The unit is $10^{-13} \text{ ergs s}^{-1} \text{ cm}^{-2}$.

|| The unit is $10^{35} \text{ ergs s}^{-1}$.

The Galactic absorption (N_H^{Gal}) was fixed to $6 \times 10^{20} \text{ cm}^{-2}$.

4 Discussion

We have performed systematic studies of the nine evolved SNRs in the Magellanic Clouds using the spatially-integrated spectra of the Suzaku XIS with uniform data reduction and spectral modeling. Despite the simpleness of our spectral modeling, we have been able to obtain the reasonable fits and the constraints on elemental abundances of the individual heavy elements. We have found the significant variation in the abundance pattern among the objects. In this section, we first describe a brief summary of the previous works to compare with our results, and then identify the best spectral feature to discriminate the progenitor type of the evolved SNRs (without spatially-resolved analysis). Finally, we discuss future prospects for ASTRO-H and beyond.

4.1 Summary of the Preceding Works and Comparison with Our Results

DEM L238 & DEM L249: Both SNRs were studied in detail with Chandra and XMM-Newton by Borkowski et al. (2006). Using the Chandra high-resolution data, they revealed that prominent Fe L-shell emission dominates the spectra from the SNR center, which suggests the SN Ia origin for the both. Our analysis also confirms the enhanced Fe abundances, whereas the abundances of the lighter elements (i.e., O, Ne, and Mg) are comparable to the mean LMC values. On the other hand,

the ionization parameters we obtained (for the high- kT_e component) are significantly lower than the previous measurements by Borkowski et al. (2006) ($\sim 10^{12} \text{ cm}^{-3} \text{ s}$).

0534–69.9 & 0548–70.4: The first detailed studies of these SNRs were made by Chandra observations (Hendrick et al. 2003). Similarly to DEM L238 and DEM L249, the SNR center spectra indicate the strong Fe L emission. Balmer-dominated optical spectra of 0548–70.4 also suggest its SN Ia origin (Smith et al. 1991). However, the O/Fe number ratio observed in this SNR is comparable to or higher than the mean LMC value (Hendrick et al. 2003), which is unusual for SN Ia ejecta composition. Our results confirm the strong Fe L emission, and reveal that the O/Fe ratio is significantly lower than the previous measurement, now reasonable as an evolved Type Ia SNR.

B0532–71.0: This SNR is associated with the HII region N206 in the LMC, and so sometimes called “the N206 SNR”. An elongated radio emission is observed between the SNR center and the east rim (Klinger et al. 2002). A nonthermal X-ray emission is associated with this feature, suggesting the presence of a pulsar wind nebula and hence a CC origin of this SNR (Williams et al. 2005). Abundance measurements were made by Chandra and XMM-Newton observations (Williams et al. 2005). Our results are basically consistent with theirs.

B0532–67.5: The only preceding study of this SNR is performed by ROSAT (Haberl & Pietsch 1999). Although XMM-Newton has also observed this SNR, the result is still unreported. We therefore analyzed the XMM-Newton image as well, determining its angular size as given in table 1. An X-ray spectrum with sufficient photon statistics has been obtained by Suzaku (i.e., this work), for the first time.

0103–72.6: This SNR is located within the HII region DEM S125 (e.g., Filipovic et al. 1998), which implies its massive star origin. The ASCA observation of this SNR confirmed its elevated metal abundances (Yokogawa et al. 2002), but the detailed chemical composition was not well constrained. The subsequent Chandra observation spatially resolved the central ejecta from the swept-up ISM shell (Park et al. 2003a). The center spectrum indicates overabundances of O and Ne, consistent with the CC scenario. Our measurement also confirms the enhanced Ne abundance even in the integrated spectrum of the entire SNR.

0049–73.6: A spatially-resolved spectral analysis was performed in detail with Chandra (Hendrick et al. 2005). The bright interior regions are dominated by O- and Ne-rich ejecta, suggesting a CC origin of this SNR, but the progenitor mass of $\gtrsim 40M_\odot$ was ruled out from the lack of a large stellar-wind bubble (which is expected for a very massive star). Similarly to 0103–72.6, we confirm the high abundances of Ne from the spatially-integrated spectral data, whereas the Fe abundance is comparable to the mean SMC value.

0104–72.3 (a.k.a. IKT 25): The progenitor type of this SNR has been controversial. Using

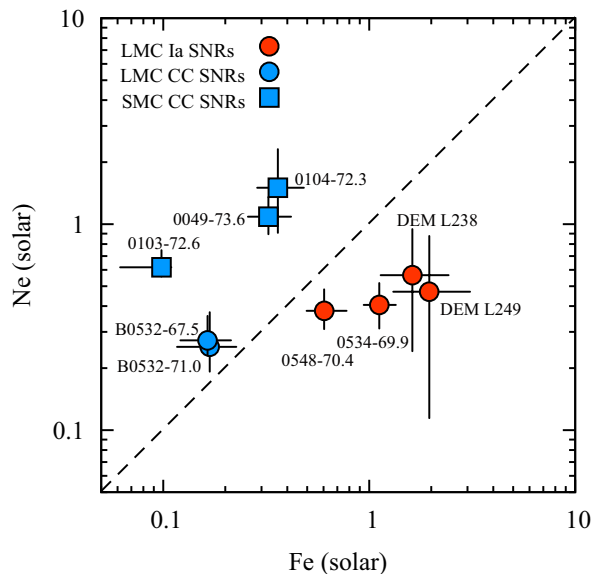


Fig. 2. Measured abundances of Fe and Ne for the SNRs in the LMC (circles) and the SMC (squares). Red and blue represent candidates of Type Ia and CC SNRs, respectively.

XMM-Newton data, van der Heyden et al. (2004) derived an overabundance of Fe, and hence proposed an SN Ia origin. This was supported by a later Chandra observation by Lee et al. (2011). However, using higher-statistics Chandra data, Lopez et al. (2014) found that the measured Ne/Fe abundance ratio is consistent with an aspherical CC SN of a massive progenitor. They therefore proposed that this SNR arose from a jet-driven bipolar SN explosion. The star formation history at the periphery of this SNR also supports the CC scenario. Our analysis indicates a high Ne/Fe ratio, supporting the latest Chandra measurement by Lopez et al. (2014). This will be discussed in more detail in the following subsections.

4.2 Typing SNRs with the Fe/Ne Abundance Ratio

As described above, we have confirmed the abundance enhancement of either Fe or the lighter elements (i.e., O, Ne and Mg) in most SNRs. For each, the progenitor type inferred from the abundance pattern agrees on the previous conclusions achieved by the spatially-resolved analysis with Chandra. This indicates that the integrated X-ray spectra of old (and thus ISM-dominant) SNRs are still contributed by the SN ejecta and thus can be used to discriminate the progenitor types with simple, unbiased spectral modeling. It should be noted that the ASCA observations of the middle-aged Magellanic SNRs (Hughes et al. 1998; see also §1) scarcely confirmed elevated metal abundances, although the soft X-ray luminosities of their targets ($L_{0.5-5\text{keV}} \approx 10^{36-37} \text{ ergs s}^{-1}$) were one or two order of magnitude higher than those of our samples (see table 2). The spectral sensitivity (i.e., effective area and

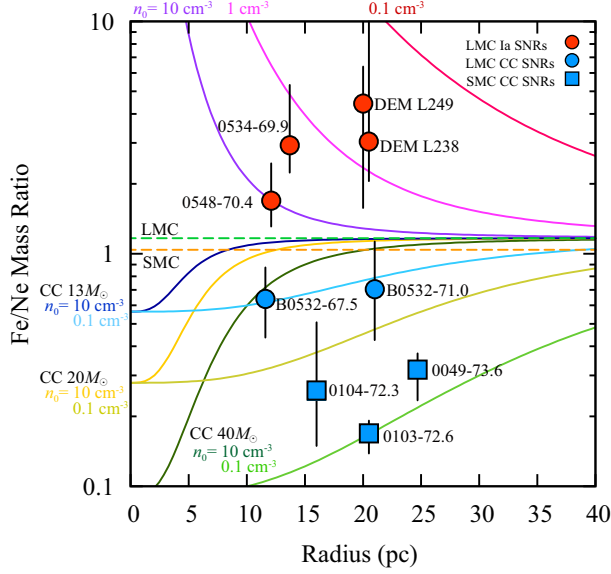


Fig. 3. Fe/Ne mass ratios as a function of the SNR radius. The mean LMC and SMC mass ratios are indicated as the dashed lines. The solid curves show the theoretical mass ratios, where both ISM and ejecta contributions are taken into account (see text for more details). For the ISM component, uniform ambient densities (n_0) of $0.1\text{--}10\text{ cm}^{-3}$ are assumed. The metal masses of the SN Ia ejecta are assumed to be those of the WDD2 model (Iwamoto et al. 1999). For the CC SNRs, we use the values predicted by Kobayashi et al. (2006) for various progenitor masses between $13 M_{\odot}$ and $40 M_{\odot}$ with a metallicity of $Z = 0.004$.

energy resolution) is, therefore, essential for precise progenitor determination particularly for X-ray faint SNRs.

The most prominent difference in the spectral feature among the nine SNRs (figure 1) is seen around 1 keV, where either Fe L-shell or Ne K-shell emission is dominant. In figure 2, we plot the measured Fe and Ne abundances (relative to H) for each SNR, clearly separating the remnants into the two distinct groups. Given this fact, we propose the Fe/Ne mass ratio as the best quantity to distinguish the progenitor type of evolved SNRs (especially when a spatially-resolved spectrum is unavailable). The merit of this ratio is also justified from the theoretical point of view. First, Fe and Ne are the major products of Type Ia and CC SNe, respectively. Second, measurements of their abundance ratio are hardly affected by a foreground extinction or an electron temperature of plasmas, because of the similar transition energies of the Fe L-shell and Ne K-shell emission. Figure 3 shows the Fe/Ne mass ratio as a function of the SNR radius. All the values are significantly higher or lower than the mean LMC/SMC values for most SNRs.

We here verify that the measured mass ratios make sense by comparing with theoretically-expected values in which the ISM contribution is taken into account. The total observed mass of Fe and Ne can be divided into those of the ISM and ejecta components as

$$\frac{M_{\text{Fe}}}{M_{\text{Ne}}} = \frac{M_{\text{ISM,Fe}} + M_{\text{ej.,Fe}}}{M_{\text{ISM,Ne}} + M_{\text{ej.,Ne}}}. \quad (1)$$

Assuming a uniform ambient density of n_0 , the Fe (and similarly Ne) mass in the ISM component is calculated as

$$M_{\text{ISM,Fe}} = m_{\text{Fe}} n_0 \left(\frac{n_{\text{Fe}}}{n_{\text{H}}} \right)_{\text{LMC}} \left(\frac{4}{3} \pi R_{\text{SNR}}^3 \right), \quad (2)$$

where m_{Fe} and $(n_{\text{Fe}}/n_{\text{H}})_{\text{LMC}}$ are the mass of single Fe atom and the mean Fe/H number ratio of the LMC (Russell & Dopita 1992). For n_0 , we consider various values in the range between 0.1 cm^{-3} and 10 cm^{-3} . The assumption of the uniform ambient density should be valid for most Type Ia SNRs (e.g., Badenes et al. 2007; Yamaguchi et al. 2014). A massive star like a red supergiant (RSG), on the other hand, usually explodes in a circumstellar matter (CSM) formed by its own pre-explosion stellar wind. However, given a typical wind velocity ($\sim 10 \text{ km s}^{-1}$) and a length of the RSG stage ($\sim 10^5 \text{ yr}$), the CSM contribution should be significant only up to a few parsecs (e.g., Dwarkadas 2005), and thus the swept-up mass of the evolved SNRs should be dominated by the pre-existing ISM. The metal masses of the ejecta component are taken from the literature values of Iwamoto et al. (1999) and Kobayashi et al. (2006) for SNe Ia and CC SNe, respectively. The calculated mass ratios as a function of the SNR radius are shown as the solid curves in figure 3. We confirm that most SNRs (both Type Ia and CC) are in good agreement with the theoretical curves.

More specifically, the mass ratios observed in the Type Ia SNRs DEML238 and DEML249 suggest their low ambient density ($\lesssim 1 \text{ cm}^{-3}$), roughly consistent with the previous measurements (Borkowski et al. 2006). On the other hand, the SNR 0548–70.4 requires a relatively high density ($\sim 10 \text{ cm}^{-3}$), which is unusual for the LMC ISM. This implies that a part of the Fe ejecta is still unshocked or forms a low-density plasma. Several CC SNRs require a high progenitor mass. However, the absolute Fe ejecta mass of a CC SN is sensitive to a ‘mass cut’ and thus known to be somewhat uncertain. In fact, we find that some other CC SN models (e.g., Thielemann et al. 1996) predict a significantly lower Fe/Ne mass ratios for any progenitor mass. Moreover, our abundance measurements are based on the phenomenological analysis with simple spectral modeling. We caution, therefore, that the plot like figure 3 should not be used to determine the accurate progenitor mass of CC SNRs, although it is definitely useful for immediate SN type discrimination.

The spectrum of 0104–72.3 is somewhat peculiar. Despite no obvious feature of Ne K emission, the derived Fe/Ne ratio is similar to the other CC SNRs. In figure 4, we show confidence contours for the abundance ratios of Fe to Ne, which is almost consistent with the previous measurements by Lopez et al. (2014). Unlike the other eight SNRs, 0104–72.3 does not require two-temperature components to fit the spectrum, but we confirm that an additional low- kT_e component (with a fixed temperature between $0.1\text{--}0.3 \text{ keV}$) does not change the Fe/Ne abundance ratio significantly. It would be worth noting that the fitting result of 0104–72.3 (figure 1) shows no residuals around 1.2 keV that

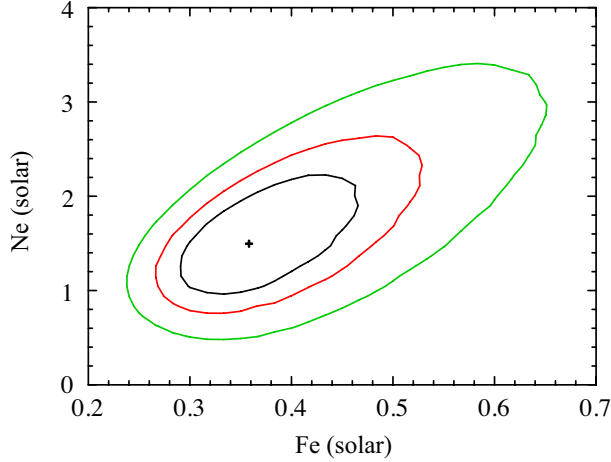


Fig. 4. Confidence contour for the abundance ratio of Fe to Ne determined from the spectrum of 0104–72.3. Black, red, and green contours are given for confidence levels of 68%, 90%, and 99%, respectively.

is commonly seen for the other Type Ia SNRs. This might be another piece of evidence for a low Fe abundance.

4.3 Future Prospects

In this work, we have proved that an Fe/Ne mass ratio determined from a spatially-integrated soft X-ray spectrum of an evolved SNR clearly discriminates its progenitor type, when with adequate energy resolution of the detector. The X-ray mission ASTRO-H will be launched in early 2016, enabling the first high-resolution spectroscopy for largely-extended sources. The evolved Magellanic SNRs are suitable targets for this mission, because the typical spatial extent of the sources is too large to be observed with a grating spectrometer but is still smaller than the field of view of the Soft X-ray Spectrometer (SXS) aboard ASTRO-H ($3' \times 3'$; Takahashi et al. 2014).

Figure 5a shows simulated SXS spectra of the SNR 0104–72.3 with an exposure of only 25 ks, where we assume our best-fit model (black) or the Fe/Ne abundance ratio reported by Lee et al. (2011) (red). The two cases (i.e., CC and Type Ia progenitor scenarios) can easily be distinguished with this short exposure time, since the strong Ly α emission expected only for the CC scenario. For the other ‘normal’ SNRs with the highest or lowest Fe/Ne ratios among our samples (i.e., DEM L249 and 0103–72.6), we can resolve the key spectral features with even shorter exposure time (5–10 ks) as demonstrated in figure 5b. A systematic study of evolved SNRs is, therefore, promising for ASTRO-H. With an ultimate X-ray mission, like Athena², we will moreover be able to perform similar studies

² The Athena mission is supposed to have a ~ 100 times larger effective area than ASTRO-H, compensating for flux decrease due to the large distance to the outer galaxies. Furthermore, because of the large distance (plus the high angular resolution of the X-ray mirror), multiple SNRs can be detected and resolved with a single pointing observations.

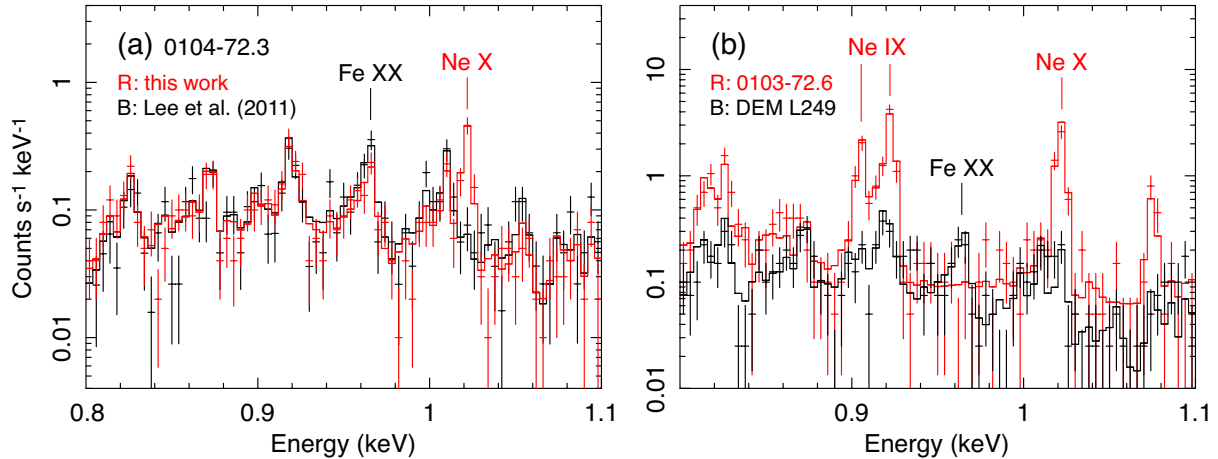


Fig. 5. (a) Simulated spectra of SNR 0104–72.3 in the 0.8–1.1 keV band for observations with the SXS aboard ASTRO-H. We use parameters of our best-fit model (see table 2) and the Fe/Ne abundance ratio reported by Lee et al. (2011) for the red and black data points, respectively. The assumed exposure time is only 25 ks for both cases. We can easily distinguish the two cases with this short exposure. (b) Simulated SXS spectra of DEM L249 (black) and 0103–72.6 (red) with the assumed exposures of 10 ks and 5 ks, respectively.

for SNRs in other nearby galaxies (e.g., M31). This will help understand the detailed chemical evolution in an entire spiral galaxy.

Finally, we should mention that the Fe/Ne-ratio diagnostic presented in this work might be valid only for Sedov-phase SNRs where the entire ejecta have already been shock-heated. In young Type Ia SNRs, on the other hand, a significant fraction of the Fe ejecta is still cool and/or in very low ionization states. In fact, Fe L emission from SN 1006 is almost invisible for this reason (Vink et al. 2003; Yamaguchi et al. 2008). For young SNRs, diagnostics using other elements (e.g., Hughes et al. 1995), X-ray morphology (Lopez et al. 2011), or ionization states of the ejecta (Yamaguchi et al. 2014) would be more useful and robust.

5 Conclusions

We have presented systematic analysis of nine SNRs in the Magellanic Clouds (DEML238, DEM L249, 0534–69.9, 0548–70.4, B0532–71.0, B0532–67.5, 0103–72.6, 0049–73.6, and 0104–72.3) observed with the Suzaku/XIS. These are all evolved SNRs with an age of $\gtrsim 10,000$ yr, so their integrated X-ray spectra in the soft X-ray band are dominated by the swept-up ISM. Nevertheless, we confirm clear signatures of the ejecta from all the observed targets. The Fe/Ne mass ratio derived from our simple unbiased spectral analysis clearly discriminates the progenitor types. DEM L238, DEM L249, 0534–69.9, and 0548–70.4 are classified as Type Ia remnants, while the other five are CC SNRs, all consistent with the previous Chandra results based on the spatially-resolved analysis. Since Fe L-shell and Ne K-shell lines are fall in the same energy range, measurements of their mass

ratio are hardly affected by a foreground extinction or plasma temperature—this is the remarkable advantage of this simple diagnostic. Future high-resolution spectroscopy with the ASTRO-H/SXS will resolve the key spectral features much more clearly with very short exposure, enabling robust systematic studies of the Magellanic Sedov-phase SNRs. This helps reveal detailed history of the recent chemical evolution in an outer galaxy.

Acknowledgments

We thank all the members of the Suzaku operation team for their continuous effort to develop and maintain the satellite. Y.T. was supported by Grant-in-Aid for the Promotion of Science (JSPS) Fellows (No. 25-5448).

References

- Arnaud, K. A. 1996, in *Astronomical Society of the Pacific Conference Series*, Vol. 101, *Astronomical Data Analysis Software and Systems V*, ed. G. H. Jacoby & J. Barnes, 17
- Badenes, C., Hughes, J. P., Bravo, E., & Langer, N. 2007, *ApJ*, 662, 472
- Borkowski, K. J., Hendrick, S. P., & Reynolds, S. P. 2006, *ApJ*, 652, 1259
- Borkowski, K. J., Hendrick, S. P., & Reynolds, S. P. 2007, *ApJL*, 671, L45
- Brickhouse, N. S., Dupree, A. K., Edgar, R. J., et al. 2000, *ApJ*, 530, 387
- Dickey, J. M., & Lockman, F. J. 1990, *ARA&A*, 28, 215
- Dwarkadas, V. V. 2005, *ApJ*, 630, 892
- Filipovic, M. D., Jones, P. A., White, G. L., & Haynes, R. F. 1998, *A&AS*, 130, 441
- Haberl, F., & Pietsch, W. 1999, *A&AS*, 139, 277
- Hendrick, S. P., Borkowski, K. J., & Reynolds, S. P. 2003, *ApJ*, 593, 370
- Hendrick, S. P., Reynolds, S. P., & Borkowski, K. J. 2005, *ApJL*, 622, L117
- Hughes, J. P., Ghavamian, P., Rakowski, C. E., & Slane, P. O. 2003, *ApJL*, 582, L95
- Hughes, J. P., Hayashi, I., & Koyama, K. 1998, *ApJ*, 505, 732
- Hughes, J. P., Hayashi, I., Helfand, D., et al. 1995, *ApJL*, 444, L81
- Iwamoto, K., Brachwitz, F., Nomoto, K., et al. 1999, *ApJS*, 125, 439
- Klinger, R. J., Dickel, J. R., Fields, B. D., & Milne, D. K. 2002, *AJ*, 124, 2135
- Kobayashi, C., Umeda, H., Nomoto, K., Tominaga, N., & Ohkubo, T. 2006, *ApJ*, 653, 1145
- Koyama, K., Tsunemi, H., Dotani, T., et al. 2007, *PASJ*, 59, S23
- Lee, J.-J., Park, S., Hughes, J. P., Slane, P. O., & Burrows, D. N. 2011, *ApJL*, 731, L8
- Lewis, K. T., Burrows, D. N., Hughes, J. P., et al. 2003, *ApJ*, 582, 770
- Lopez, L. A., Castro, D., Slane, P. O., Ramirez-Ruiz, E., & Badenes, C. 2014, *ApJ*, 788, 5

Lopez, L. A., Ramirez-Ruiz, E., Huppenkothen, D., Badenes, C., & Pooley, D. A. 2011, *ApJ*, 732, 114

Park, S., Hughes, J. P., Burrows, D. N., et al. 2003a, *ApJL*, 598, L95

Park, S., Hughes, J. P., Slane, P. O., et al. 2003b, *ApJL*, 592, L41

Russell, S. C., & Dopita, M. A. 1992, *ApJ*, 384, 508

Serlemitsos, P. J., Soong, Y., Chan, K.-W., et al. 2007, *PASJ*, 59, 9

Smith, R. C., Kirshner, R. P., Blair, W. P., & Winkler, P. F. 1991, *ApJ*, 375, 652

Takahashi, T., Mitsuda, K., Kelley, R., et al. 2014, in *Society of Photo-Optical Instrumentation Engineers (SPIE) Conference Series*, Vol. 9144, *Society of Photo-Optical Instrumentation Engineers (SPIE) Conference Series*, 25

Thielemann, F.-K., Nomoto, K., & Hashimoto, M.-A. 1996, *ApJ*, 460, 408

Uchida, H., Koyama, K., & Yamaguchi, H. 2015, *ApJ*, 808, 77

van der Heyden, K. J., Bleeker, J. A. M., & Kaastra, J. S. 2004, *A&A*, 421, 1031

Vink, J. 2012, *A&AR*, 20, 49

Vink, J., Laming, J. M., Gu, M. F., Rasmussen, A., & Kaastra, J. S. 2003, *ApJL*, 587, L31

Westerlund, B. E. 1990, *A&AR*, 2, 29

Williams, R. M., Chu, Y.-H., Dickel, J. R., et al. 2005, *ApJ*, 628, 704

Yamaguchi, H., Koyama, K., Katsuda, S., et al. 2008, *PASJ*, 60, S141

Yamaguchi, H., Badenes, C., Petre, R., et al. 2014, *ApJL*, 785, L27

Yokogawa, J., Imanishi, K., Koyama, K., Nishiuchi, M., & Mizuno, N. 2002, *PASJ*, 54, 53